Improved ion beam tools for ultraprecision figure correction of curved aluminum mirror surfaces

Jens Bauer
Melanie Ulitschka
Fred Pietag
Thomas Arnold

SPIE.

Improved ion beam tools for ultraprecision figure correction of curved aluminum mirror surfaces

Jens Bauer,[a,*] **Melanie Ulitschka,**[a] **Fred Pietag,**[a] **and Thomas Arnold**[a,b]
[a]Leibniz Institute of Surface Engineering (IOM), Leipzig, Germany
[b]Technische Universität Dresden, Institute of Manufacturing Science and Engineering, Germany

Abstract. Aluminum mirrors offer great potential for satisfying the increasing demand in high-performance optical components for visible and ultraviolet applications. Ion beam figuring is an established finishing technology and in particular a promising technique for direct aluminum figure error correction. For the machining of strongly curved or arbitrarily shaped surfaces as well as the correction of low-to-mid spatial frequency figure errors, the usage of a high-performance ion beam source with low tool width is mandatory. For that reason, two different concepts of ion beam generation with high ion current density and narrow beam width are discussed. (1) A concave ion beam extraction grid system is used for apertureless constriction of ion beams in the low millimeter range. An oxygen ion beam with a full-width at half-maximum (FWHM) of 4.0 mm with an ion current density of 29.8 mA/cm^2 was achieved. (2) For even smaller ion beams, a conic aperture design with a submillimeter-sized exit opening was tested. A nitrogen ion beam with an FWHM down to 0.62 mm with an ion current density of 4.6 mA/cm^2 was obtained. *In situ* ion current density mapping is performed by scanning Faraday probe measurements. Special interest is set on the data evaluation for submillimeter ion beam analysis. © *The Authors. Published by SPIE under a Creative Commons Attribution 3.0 Unported License. Distribution or reproduction of this work in whole or in part requires full attribution of the original publication, including its DOI.* [DOI: 10.1117/1.JATIS.4.4.046003]

Keywords: ion beam figuring; submillimeter ion beam tools; ion optical components; Faraday probe analysis.

Paper 18040 received Jun. 4, 2018; accepted for publication Oct. 25, 2018; published online Nov. 13, 2018; corrected Nov. 15, 2018.

1 Introduction

Modern short-wavelength imaging systems in the visible and ultraviolet spectral range are based upon complex figured mirror devices with a spherical, aspherical, or free-form surface shape.[1] A widely used finishing technique for most precise optical devices is ion beam figuring.[2–4] Recently, it has been shown that the application of reactively driven, low-energy ion beam tools allows the direct figure error correction of mirror optics made from aluminum technical alloy materials AL6061 or AL905.[5,6] Nontoxic gases as oxygen and nitrogen are used for ion beam processing. In contrast to the usual understanding of reactive ion beam etching (RIBE), no volatile reaction products are formed during operation. But the surface is chemically modified in a characteristic manner. As a result of ion implantation, an about 10- to 15-nm thick surface oxide or nitride layer is formed depending on the process gas used. The erosion process rests upon pure physical sputtering within this surface layer, enabling a high degree of process control.[6] With this innovative technology, it is now possible to correct the figure error of the mirror surfaces up to 1 μm in height while preserving the surface roughness. Hence, costly additional processing sequences providing an isotropic surface layer of amorphous silicon or nickel-phosphorous[7] to achieve a smooth surface after ion beam figuring are not necessary. Furthermore, the applicability of aluminum mirrors with an isotropic surface layer is often limited, because the bimetal effect has to be considered. Severe issues can result from typical mirror applications, such as device bending in light-weight design devices or even cracking of the isotropic surface layer under rough application conditions such as thermal load. Furthermore, direct aluminum surface

processing allows utilization of the high broadband reflectance from the ultraviolet (UV) over the visible (VIS) to the infrared (IR) spectral range with values well above 90% directly to the application. Especially, in the UV–VIS range, the reflectance values of amorphous silicon and nickel-phosphorous are usually not sufficient so that an additional metalization is mandatory. Those extensive mirror fabrication steps are not needed in a direct finishing scheme. However, one major issue of ion beam figuring is the low processing speed, especially in the case of reactive processing of aluminum surfaces. Compared to the standard ion beam figuring with argon gas, the material removal rate is reduced in the oxygen process by a factor of 5 and in the nitrogen case to the half. Hence, it would be most desirable to increase the process efficiency by a rise of the ion current density provided by the ion beam tool maintaining a small beam width and a Gaussian beam shape.

Optical aluminum surfaces are usually fabricated by single-point diamond turning (Fig. 1). By the state-of-the-art, a root-mean-square (rms) roughness of 2 to 3 nm is achievable.[8,9] Those surfaces are perfectly appropriate for IR applications.[10,11] In addition, reactive ion beam technology can be used to improve figure accuracy. However, optics for use in the VIS and UV spectral range demands even better surface qualities. Roughness values of 1 and <0.3 nm rms need to be targeted, respectively.[2] The reactive ion beam figuring technology allows the preservation of the initial surface topography[5,6] but not to improve the surface properties. Hence, the required surface qualities need to be provided prior to ion beam figuring. Since single point diamond-turning is not sufficient, advanced polishing technologies have to be developed. For the correction of waviness and microroughness errors, ion beam planarization is an established technique.[12] In particular, an ultrasmooth sacrificial layer is coated homogeneously onto the rough device surface. Under special process conditions, i.e., under a specific

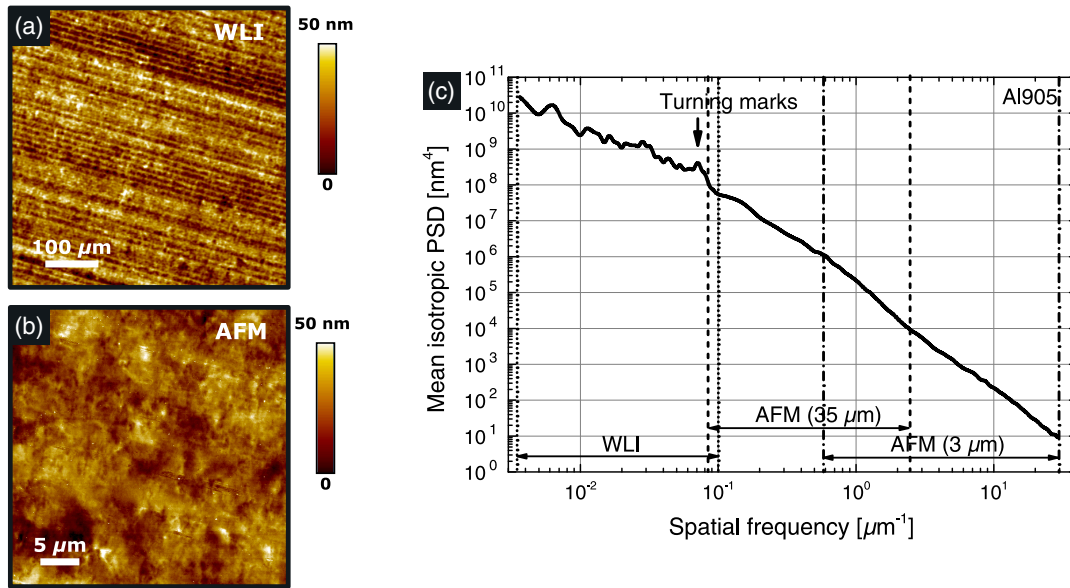*Address all correspondence to: Jens Bauer, E-mail: jens.bauer@iom-leipzig.de

Fig. 1 Optical AL905 surface after diamond-turning measured by (a) white light interferometry (WLI) and (b) atomic force microscopy (AFM). (c) The isotropic power spectral density function was determined as the mean from 5× measurements of each measurement set (WLI as well as AFM with scanning field sizes of 35 and 3 μm). Characteristic turning mark features are apparent at the spatial frequency 0.071 μm^{-1}. The surface roughness within $(3 \cdot 10^{-3} - 3 \cdot 10^{1})$ μm^{-1} is (4.7 ± 0.8) nm rms.

machining angle or with a specific process gas composition, the removal rate of the sacrificial layer is equal to that of the substrate material. As a result, the ultrasmooth surface can be transfered into the device surface. Ion beam planarization with reactive process control seems to be a promising technique for smoothing of aluminum mirror devices, in particular by the reduction of turning mark features and microroughness.

For reasons of device shape flexibility, a deterministic machining approach with a small-sized tool function as well as a considerable beam current density is desirable also for a prospective ion beam planarization technology.

For figure error correction, the process sequence is as follows: first, a dwell-time algorithm is applied to transfer the figure error profile into a motion map. Following this simulated
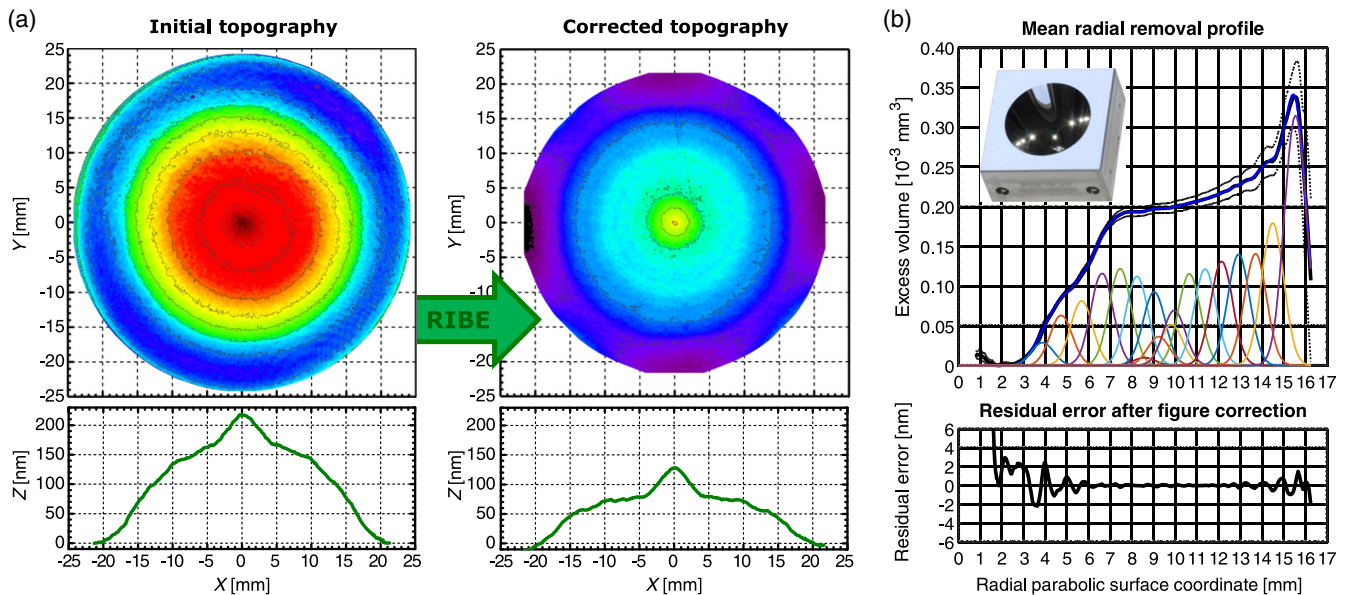

Fig. 2 (a) RIBE correction of a planar AL905 mirror optics: figure error profile before and after RIBE correction measured by interferometry. For RIBE processing, a crossed-machining procedure was applied to achieve a best-fit paraboloidal correction with about 100-nm central removal.[5] (b) RIBE process simulation of a paraboloidal imaging mirror optics made of AL905: the figure error after diamond turning is radial symmetric. Hence, an isotropic error profile along the radial parabolic surface coordinate (black solid; coincidence bands dotted) is calculated. The best-fit removal profile (blue solid) is determined by simulation of 18 discrete ring RIBE machining steps. The calculated residual error is <5 nm PV.[13]

motion profile, the ion beam is then moved deterministically along the device surface. This approach allows the figure error correction of huge and diversely shaped mirror devices. The smaller the tool size, the higher the flexibility in the device shape and the higher the spatial frequency features to be reached during correction.

An example for RIBE figure error correction is shown in Fig. 2(a). The planar aluminum mirror has a concentric figure error profile as a result of the diamond turning process. For the first rough correction, a best-fit paraboloidal removal with a 1.5-keV nitrogen ion beam was performed. A free ion beam without use of an aperture was applied benefiting from a high beam intensity at a moderate full-width at the half-maximum (FWHM) of 5.2 mm.[5]

The concave parabolic mirror in Fig. 2(b) has an aspect ratio of central depth to open aperture of $\approx$0.6. Presently, only the ion beam figuring technology may allow the correction of a deep aluminum optical device like this. Since the figure error has a concentric shape, a radial symmetric machining scheme is advantageous. For that reason, the sample is rotated fast around the paraboloid axis. The ion beam is directed at normal incidence to the surface at different discrete distances along the parabolic surface coordinate (R). As a result, at each position, a discrete ring removal is obtained [Fig. 2(b)]. However, an ion beam tool with an FWHM of at least 1.2 mm is necessary to allow the correction of the narrow main error feature at about $R = 15.5$ mm. An appropriate subaperture ion beam has to be used for the successful mirror device correction.

Hence, the generation of intense millimeter- and submillimeter-sized ion beams is key for the successful realization of figure error correction and ion beam planarization of curved optics. In the following, first the conception of ion beam constriction by concave-shaped beam extraction grids is focussed (Sec. 2). Then, subaperture conceptions as the conventional pinhole aperture (Sec. 3.2) and a contraction aperture design (Sec. 3.3) are evaluated.

2 Shaping of the Free Ion Beam

A 13.56-MHz transformer coupled plasma (TCP)-type ion beam source[14] is driven by inert (Ar) or reactive (O_2 and N_2) process gas [Fig. 3(a)] at a beam voltage $\leq$1.5 keV. The ion extraction and beam formation are performed by a triple grid system (G1-3). The grids are spherically concave shaped. As a result, the ion beam exhibits a constricted region. The working distance is chosen as the point of maximum constriction, i.e., at the smallest beam width. The beam constriction and the working distance can be tuned by adjustment of the grid curvature. Figures 3(b) and 3(c) show Faraday probe measurements at optimized ion beam conditions with altered grid curvature radius. The corresponding process parameters are summarized in Table 1. For a curvature radius of 150 mm [Fig. 3(b)] the ion extraction was limited by a screen grid (G1) opening of 10 mm. As a result, a narrow ion beam with 5.1 mm beam width and a strong ion current density of 8.1 mA/cm² is obtained. An improved constriction is achieved by a curvature radius of 100 mm [Fig. 3(c)]. Despite an increased screen grid opening of 20 mm, i.e., an increase of the ion extraction area by a factor of 4, the beam constriction is much improved. Thus, the beam width in the

Table 1 Constriction engineering of the free ion beam by adjustment of the extraction grid curvature.

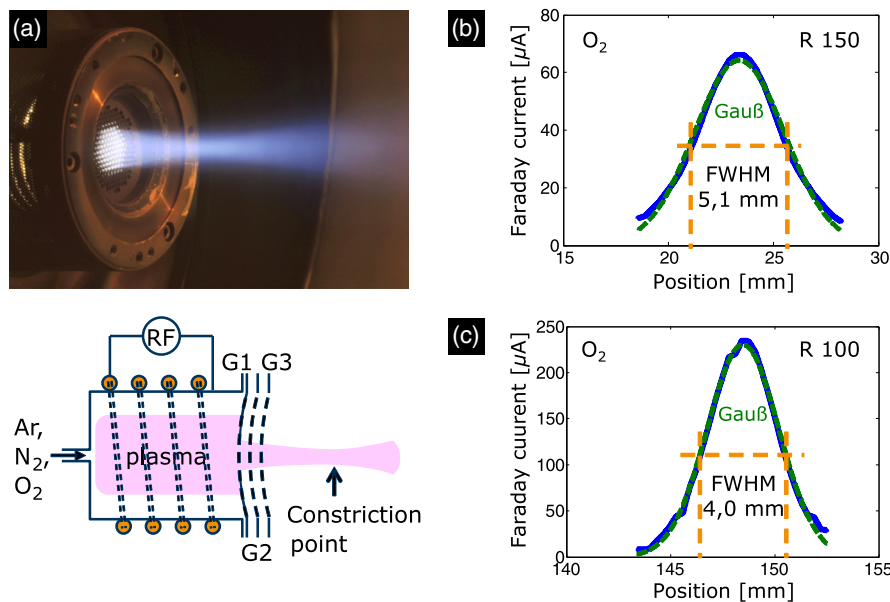| Grid curvature radius	$R = 150$ mm	$R = 100$ mm
Screen grid opening	10 mm	20 mm
Working distance	32 mm	55 mm
Beam width (FWHM)	5.1 mm	4.0 mm
Beam shape	Gauss	Gauss
Ion current density	$j = 8.1$ mA/cm²	$j = 29.8$ mA/cm²

Fig. 3 (a) TCP-type ion beam source with concave-shaped extraction grids (curvature radius R) resulting is a constriction of the ion beam. (b/c) Faraday probe measurements of 1.5-keV oxygen ion beams at the working distance for grid curvature radius (b) $R = 150$ mm and (c) $R = 100$ mm.

constriction point is with 4.0 mm, even smaller than for the 150-mm curvature radius grid system. The ion current density scales with the ion extraction area to 29.8 mA/cm^2. Furthermore, the working distance is increased to 55 mm for the 100-mm curvature radius case. A higher working distance allows better flexibility in sample positioning in front of the ion source during ion beam processing.

Consequently, all process parameters indicate a much better performance for the 100-mm grid system over the 150-mm grid system. However, there is one major drawback since the operation life-time for the 100-mm grid system is more limited. In particular, the 150-mm grid system shows a stable operation over months while the 100-mm grids are strongly eroded within a few weeks accompanied by a considerable process parameter drift. Especially in production environments, this disadvantage can strongly reduce cost efficiency. For the forthcoming results on subaperture ion beams, the 150-mm grid system was applied.

3 Subaperture Ion Beams

3.1 *Faraday Probe Analysis of Subaperture Ion Beams*

Usually the data evaluation during Faraday probe analysis is a straightforward process since the measured current density directly represents the ion current density at the probe position. A Gaussian beam profile with total ion current I$_{total}$ is given as

$$J(x, y) = \frac{1}{2\pi\sigma^2} I_{\text{total}} \cdot e^{\left[-\frac{1}{2\sigma^2}(x^2 + y^2)\right]}. \tag{1}$$

The variance (σ) is a measure for the beam width: FWHM $= 2\sqrt{2\ln(2)} \cdot \sigma$. This situation changes drastically if the ion beam width is in the order of the probe aperture opening or even below. Then, the data evaluation is more difficult. There are three regimes to be considered for proper data evaluation of Faraday probe measurements (Fig. 4):

1. In the limit, in which the beam width is much smaller than the Faraday probe aperture (d), the top hat-like aperture profile determines the shape of the measurement profile [Fig. 4(a)]. As a result of the beam

width, the top hat edges are rounded. The rounding can be mathematically described by a Gaussian error function (left flank at position $-d/2$)

$$I(x) = \frac{1}{2} I_{\text{total}} \left\{ 1 + \text{erf}\left[\sqrt{2}\sigma\left(x + \frac{d}{2}\right)\right] \right\}, \tag{2}$$

while the variance (σ) is equal to the variance of the Gaussian-like ion beam current density function [Eq. (1)].

2. In the case if ion beam width and Faraday probe aperture are in the same order, the measurement profile is the convolution of beam profile (J) and the aperture top hat profile (A):

$$I(x) = (J * A)(x) \tag{3}$$

As shown in Fig. 4(b), a pure Gaussian fit of the measurement profile would deliver a too broad beam width and too low ion current density in the beam center.

3. For a broad ion beam, the narrow Faraday probe allows scanning the ion beam profile directly [Fig. 4(c)].

To account for the experimental conditions, a two-dimensional (2-D) convolution model with a circular probe aperture ($\varnothing_{\text{probe}}$) and a Gaussian bell curve [Eq. (1)] as the actual beam profile has to be considered. The general behavior in the 2-D case follows the one-dimensional (1-D) case [Fig. 5(a)]. The scaling for the experimental conditions can be expressed by the scaling exponent m: FWHM$_{\text{measured}}$/FWHM$_{\text{beam}}$ $\propto$ (FWHM$_{\text{beam}}$)^m [Fig. 5(b)]. For a circular Faraday probe opening of 1.0 mm diameter, the systematic measurement uncertainty of the measured profile width is well below 2% for a beam width ≥ 3.0 mm (Table 2). For narrow ion beams with a FWHM < 3.0 mm, which is usually the case if an aperture is applied, a deconvolution of the measured profile with the circular Faraday probe top hat profile is necessary.
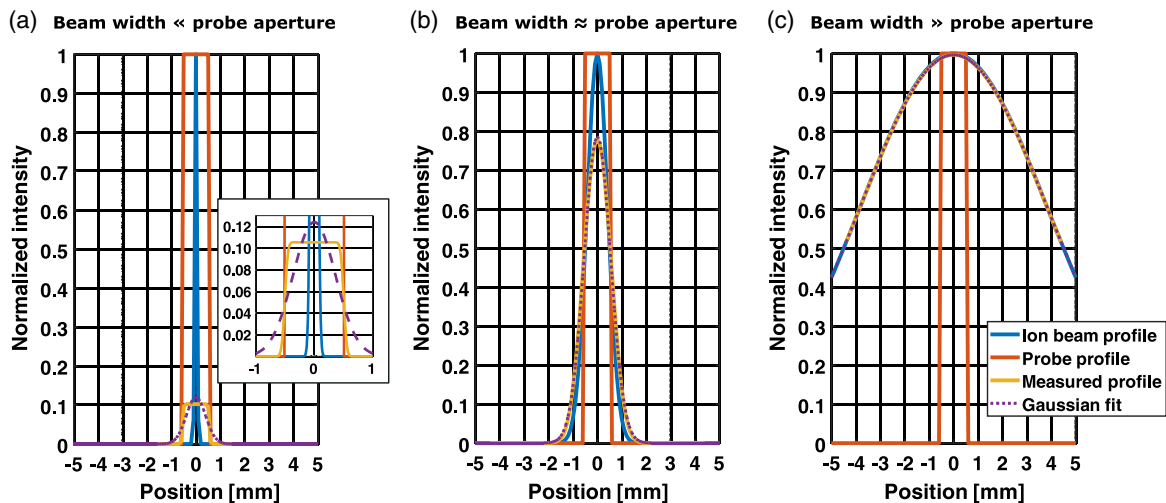

Fig. 4 Illustration of the data evaluation during Faraday analysis (1-D model) for (a) a very narrow ion beam, (b) an ion beam width in the order of the probe aperture, and (c) a broad ion beam.
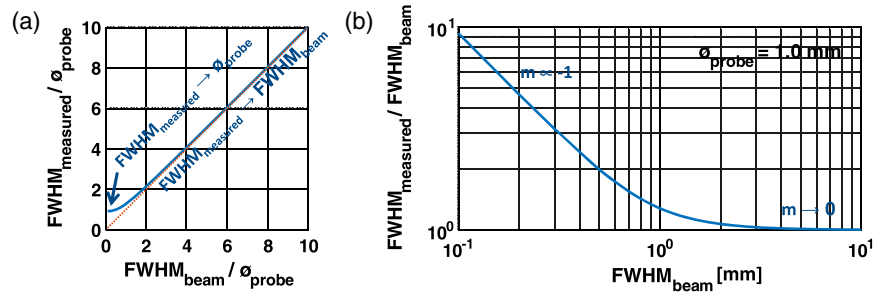
Fig. 5 2-D convolution model: (a) corresponding to the 1-D case (Fig. 4) the convolved profile of the Faraday probe measurement deviates from the actual beam profile for beam widths in the order of the Faraday probe diameter or below. (b) Ratio of convolved profile width to the actual beam profile width with respect to the beam width for the experimental case of a probe aperture opening of 1.0 mm.

Table 2 Ratios of beam width (FWHM) and beam current (I) between measured (convolved) profile and actual beam profile for a circular Faraday probe opening of 1.0 mm diameter.

$FWHM_{beam}$	$FWHM_{measured}/FWHM_{beam}$	$I_{measured}/I_{beam}$
1.0 mm	118.0%	72.5%
2.0 mm	104.4%	91.9%
3.0 mm	101.9%	96.3%

3.2 Pinhole Aperture

The simplest way to produce millimeter and submillimeter ion beams is the use of a pinhole aperture.[15] Only the part of the ion beam in the area of the pinhole can pass the aperture, the residual portion of the ion beam gets lost. As a result, the beam width is strongly reduced, but unfortunately the ion current is lowered due to the beam shading. Another disadvantage is a possible sample contamination by particles or deposit, which results from sputtering of the residual ion beam portion when hitting the aperture.

An example of a 0.8-mm pinhole aperture is shown in Fig. 6. The beam width is 1.2 mm (FWHM) at a working distance of 4 mm. However, the ion current density is 0.17 mA/cm^2, which is unacceptably low for an efficient surface figuring process. Also, the short working distance is problematic since the sample movement is strongly limited. Especially complex shaped or deep optical devices as in Fig. 2 are not machinable with the pinhole aperture conception.

3.3 Contraction Aperture

To face the strong drawbacks of a conventional pinhole aperture, an ion beam contraction aperture design was tested. The basic idea is to continuously contract the ion beam by successive side wall narrowing. For that reason, a slim conic shaped aperture was fabricated [Fig. 7(a)]. Because of its low sputtering yield, graphite was chosen as base material. The cone angle was 20 deg. Hence, the ions impinge the cone surface under grazing conditions (ion incidence angle >80 deg toward the normal),
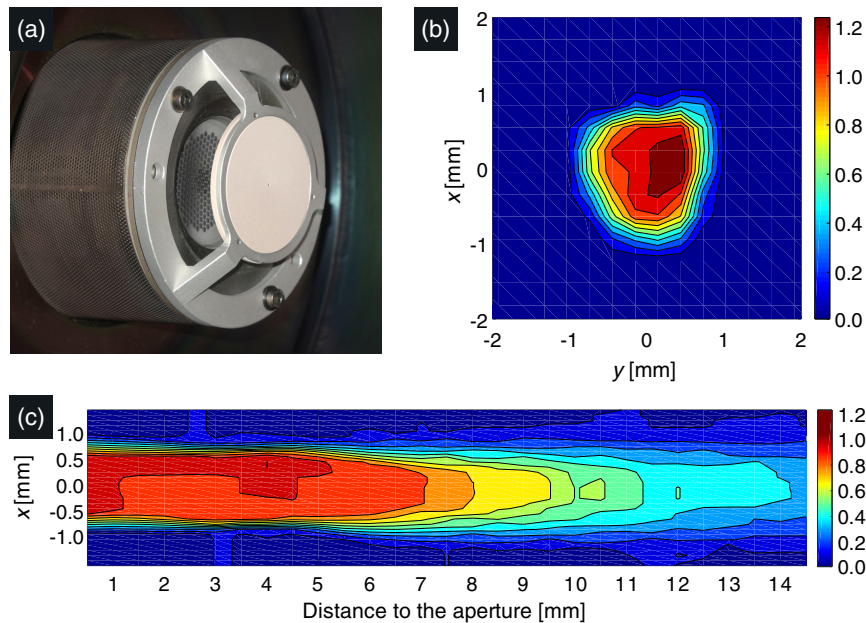

Fig. 6 (a) Ion beam source with attached pinhole aperture. The pinhole diameter is 0.8 mm. (b) Cross-sectional Faraday probe measurement of an 1.5-keV oxygen ion beam at 0.5 mm distance to the aperture and corresponding (c) in-plane Faraday probe measurement.
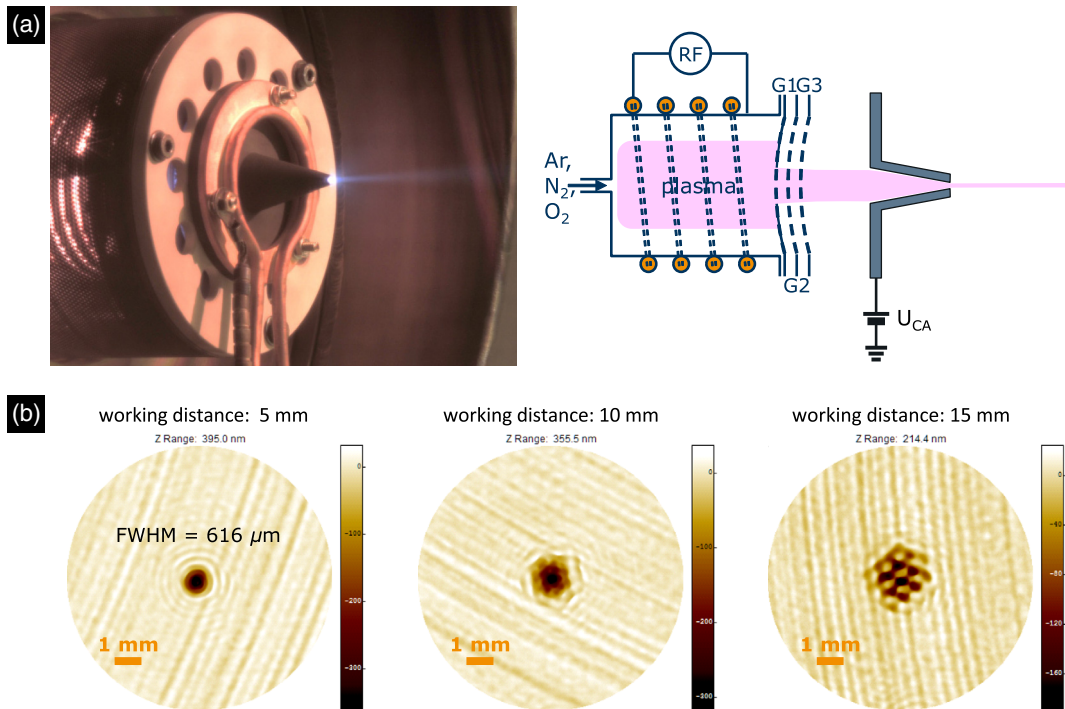
Fig. 7 (a) Ion beam source with attached contraction aperture. The exit pupil diameter is 0.885 mm. (b) Interferometer images of footprint etchings in Al905 from a 1.5-keV nitrogen ion beam at different working distances.

so the ions are almost reflected while sputtering of the side walls is of inferior significance. However, secondary electron production is increased under those geometric conditions. Thus, the aperture was mounted onto a ceramic adapter plate to allow the application of a positive DC voltage $U_{CA} < 10$ V during operation. For reasons of thermal management, an active water cooling was used. The exit opening of the contraction aperture is in the range 0.5 to 3.0 mm.

Footprint etching tests showed a very good performance of the contraction aperture design [Fig. 7(b)]. With a 0.885-mm aperture opening, an ion beam width of 0.616 mm (FWHM) was obtained at 5 mm working distance. Increasing the working distance results in a beam width broading. But besides that, a distinct beam modulation structure becomes apparent, which results from the beamlet configuration of the ion beam. Hence, the aperture acts not as a diffuse ion contractor but as a narrow ion lens optics.

The ion beam was analyzed by Faraday in-plane measurements [Fig. 8(a)]. The applicability of the deconvolution method (Sec. 3.1) was verified by the analysis of the fitting residuum map as shown in Fig. 8(b). The central residual ion current distribution increase near the aperture (1- to 5-mm distance region) indicates an ion beam profile, which is narrower than an ideal Gaussian function. Oppositely, in the 9- to 14-mm distance range, the central residual ion current distribution is slightly lowered, i.e., compared to an ideal Gaussian the beam profile is broadened to some extent. All in all the residuum is almost below 10% compared to the measured ion current distribution in Fig. 8(a) legitimizing the approach for application in submillimeter-sized ion beam analysis.

The beam width obtained by the Faraday analysis correlates well with the width of the footprint etchings at working

distances <7 mm [Fig. 8(c)]. For higher working distances deviations become apparent, which probably result from the modulated beam structure. Next to the aperture opening, the beam width is narrowest with about 0.5 mm. Furthermore, the ion beam current was found to be fairly constant over a broad working distance range up to 18 mm distance from the aperture [Fig. 8(d)]. This result correlates well with the constant removal rate obtained from the footprint etchings. The beam current density was 4.6 mA/cm^2 representing the high efficiency of the contraction aperture design.

In summary, two concepts for small-sized ion beam generation have been presented: (1) aperture-free ion beams with a tool width in the range of a few millimeters can be generated by use of concave-shaped extraction grids. This conception allows high beam current densities up to about 30 mA/cm^2 and thus high processing rates. Since there is no aperture, potential contaminations as deposited layers or particles resulting from the aperture can be avoided. Due to the high beam currents, this tool allows an efficient processing of low-spatial frequency figure errors. Residual higher frequency errors can then be processed by the subaperture ion beam technique. (2) Highly intense submillimeter ion beams can be produced by the contraction aperture concept. The slim conic aperture design allows ion beam processing near the aperture opening in the high-efficiency ion beam region. The high-beam current density of about 4.6 mA/cm^2 makes deterministic, ultraprecision machining with submillimeter ion beams interesting for figure correction of diversely shaped aluminium devices, e.g., spherical, aspherical, freeform, or even strongly curved optical surfaces. Furthermore, the improved ion beam tool concepts can be a starting point for the desirable development of efficient ion beam planarization process schemes, which would be most
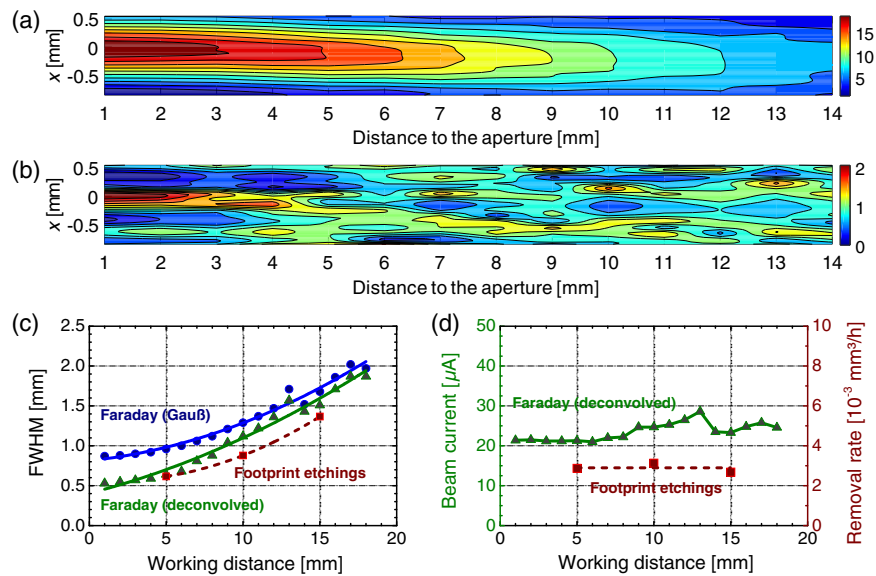
Fig. 8 (a) In-plane ion current distribution obtained by Faraday probe measurements of a 1.5-keV nitrogen ion beam by usage of the contraction aperture in Fig. 7. (b) Residuum of the ion current distribution after deconvolution with the 1-mm wide Faraday probe top hat profile and Gaussian beam fitting. (c) Ion beam width and (d) ion beam current derived from the Faraday analysis. For comparison the widths of the footprint etchings [Fig. 7(b)] and the obtained removal rates are added to (c) and (d), respectively.

interesting for aluminum mirror devices applied in the UV–VIS spectral range. This study focuses on exemplary ion beam finishing of aluminum mirrors, since aluminium is a most important mirror construction material. However, the utilization of the described ion beam tools is not expected to be limited to aluminum. Future investigations are encouraged to evaluate the prospective performance enhancement of deterministic ion beam technologies by the presented ion beam tool concepts, using materials other than aluminum.

Acknowledgments

References

1. F. Z. Fang et al., "Manufacturing and measurement of freeform optics," *CIRP Ann.* **62**(2), 823–846 (2013).
2. M. Weiser, "Ion beam figuring for lithography optics," *Nucl. Instrum. Methods Phys. Res. Sect. B* **267**(8–9), 1390–1393 (2009).
3. M. Zeuner and S. Kiontke, "Ion beam figuring technology in optics manufacturing," *Opt. Photonik* **7**, 56–58 (2012).
4. L. Zhou et al., "One-dimensional ion-beam figuring for grazing-incidence reflective optics," *J. Synchrotron Radiat.* **23**, 182–186 (2016).
5. J. Bauer et al., "Figure error correction of aluminium mirrors by deterministic reactive ion-beam machining," in *EOS Optical Technologies: 5th Conf. on Manufacturing of Optical Systems*, European Optical Society, Munich, Germany (2017).
6. J. Bauer, F. Frost, and T. Arnold, "Reactive ion beam figuring of optical aluminium surfaces," *J. Phys. D* **50**, 085101 (2017).
7. Y. Li, H. Takino, and F. Frost, "Characteristics of diamond turned NiP smoothed with ion beam planarization technique," *J. Eur. Opt. Soc.* **13**(1), 27 (2017).
8. G. P. H. Gubbels, B. W. H. Venrooy, and R. Henselmans, "Accuracy of freeform manufacturing processes," *Proc. SPIE* **7426**, 742607 (2009).
9. D. Vukobratovich and J. P. Schaefer, "Large stable aluminum optics for aerospace applications," *Proc. SPIE* **8125**, 81250T (2011).
10. M. Suganuma et al., "Aluminum-made 5-cm reflecting telescope for nano-JASMINE," *Proc. SPIE* **6265**, 626545 (2006).
11. I. J. Saunders et al., "Fabrication and metrology of freeform aluminum mirrors for the SCUBA-2 instrument," *Proc. SPIE* **5869**, 586905 (2005).
12. F. Frost et al., "Smoothing of diamond-turned copper surfaces using ion beams with aid of planarizing film," *Jpn. J. Appl. Phys.* **46**, 6071–6073 (2007).
13. J. Bauer et al., "Ultra-precision surface figuring of optical aluminium devices," in *OSA Advanced Photonics Congress*, I. Aggarwal et al., Eds., Optical Society of America, Zurich, Switzerland (2018).
14. M. Zeuner et al., "Optimisation and characterization of a TCP type RF broad beam ion source," *Surf. Coatings Technol.* **142**–**144**, 39–48 (2001).
15. T. Hänsel et al., "Ultra-precision surface finishing by ion beam techniques," *Vak. Forsch. und Prax.* **19**(5), 24–30 (2007).

Jens Bauer received his diploma degree in physics from the University of Leipzig, Germany. He finished his PhD studies at the Institute of Inorganic Chemistry at the University of Leipzig in 2009. Afterward, he worked in institutional research as well as in several companies with focus on nanomaterial and thin film technology. Since 2014, he has been acting as a development engineer for optical device finishing by ion beam technologies at the Leibniz Institute of Surface Engineering (IOM) in Leipzig.

Melanie Ulitschka studied in the engineering sciences bachelor's program in industrial engineering, specializing in material engineering

and plastics technology and master's program in composite materials at Hof University of Applied Science. From 2015 to 2017, she worked as a research assistant at the Institute for Materials Science at Hof. Since 2017, she has been engaging in ion beam technologies as a research assistant and doctoral candidate at the Leibniz Institute of Surface Engineering (IOM) in Leipzig.

Fred Pietag studied physics at the University of Leipzig. He received his diploma for working in a photoluminescence laboratory mainly dealing with $A^{III}B^{V}$-semiconductors before he was hired by a machine-building company producing machinery for ion-beam etching. Later, he was hired by the current Leibniz Institute of Surface Engineering (IOM). His main expertise now is ion-beam figuring and fast switching electronics.

Thomas Arnold studied physics and has gained his doctoral degree from Leipzig University, Germany in 2005. Since 2008, he has been the head of nonconventional ultraprecision surface machining work group with Leibniz Institute of Surface Engineering (IOM), Germany. Since 2014, he has been an endowed professor of ultraprecision surface machining using ions and plasmas at the Technical University Dresden, Germany. His main research interests are plasma-related surface machining technologies, optical manufacturing, and measurement.